

Compensated Ferrimagnets with Colossal Spin Splitting in Organic Compounds

Taiki Kawamura¹, Kazuyoshi Yoshimi², Kenichiro Hashimoto³, Akito Kobayashi¹, and Takahiro Misawa^{2*}

¹Department of Physics, Nagoya University, Nagoya, Aichi 464-8602, Japan

²Institute for Solid State Physics, University of Tokyo, Kashiwa, Chiba 277-8581, Japan

³Department of Advanced Materials Science, University of Tokyo, Kashiwa, Chiba 277-8561, Japan

The study of the magnetic order has recently been invigorated by the discovery of exotic collinear antiferromagnets with time-reversal symmetry breaking. Examples include altermagnetism and compensated ferrimagnets, which show spin splittings of the electronic band structures even at zero net magnetization, leading to several unique transport phenomena, notably spin-current generation. Altermagnets demonstrate anisotropic spin splitting, such as d -wave, in momentum space, whereas compensated ferrimagnets exhibit isotropic spin splitting. However, methods to realize compensated ferrimagnets are limited. Here, we demonstrate a method to realize a fully compensated ferrimagnet with isotropic spin splitting utilizing the dimer structures inherent in organic compounds. Moreover, based on *ab initio* calculations, we find that this ferrimagnet can be realized in the recently discovered organic compound (EDO-TTF-I)₂ClO₄. Our findings provide an unprecedented strategy for using the dimer degrees of freedom in organic compounds to realize fully compensated ferrimagnets with colossal spin splitting.

Introduction.—Collinear antiferromagnets have traditionally been viewed as conventional magnetic orderings that lack unique phenomena such as spin current generation. However, recent theoretical advances have identified exotic collinear antiferromagnets with time-reversal breaking, notably altermagnets [1–3] and compensated ferrimagnets [4]. These magnetic states exhibit spin splitting in their electronic band structures even without net magnetization. Because spin splitting may drive spin-dependent novel transport phenomena and unconventional superconducting phases, these distinctive antiferromagnets have attracted considerable attention.

Several materials have been proposed as candidates for altermagnetism [3, 5–13]. For example, κ -ET-type organic compounds [6] and transition metal oxide RuO₂ [8, 10, 14] exhibit altermagnetism with anisotropic spin splitting in electronic band structures. These materials are expected to exhibit spin-dependent transport and anomalous Hall effects owing to anisotropic spin splitting. In contrast, compensated ferrimagnets offer isotropic spin splitting, increasing efficiency for spin-current generation. The concept of metallic compensated ferrimagnetism (half-metallic antiferromagnetism) was introduced by van Leuken and de Groot [15]. Since then, several candidate materials have been suggested using *ab initio* calculations [16, 17]. More recently, monolayer MnF₂ was proposed as an insulating compensated ferrimagnet [18]. Since the magnetic moment of compensated insulating ferrimagnets is strictly zero due to the Luttinger theorem [4], small perturbations do not change the compensation condition. In addition, compensated ferrimagnets have lower crystal symmetry than altermagnets [4]. Therefore, compensated ferrimagnets have advantages over altermagnets, leading to various potential applications, such as thin-film synthesis. However, the number of compensated ferrimagnets discovered experimentally is limited [19–22]. To harness the compensated

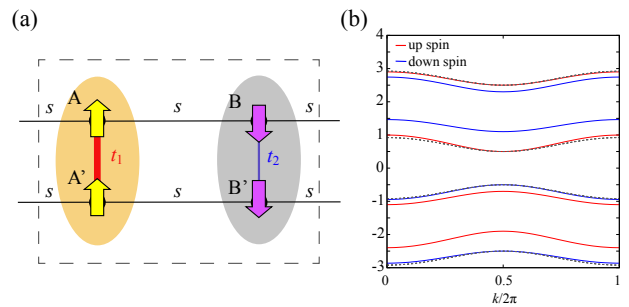


FIG. 1. (a) Schematic of a one-dimensional model showing the compensated ferrimagnetism. The broken lines show a unit cell. The inter-dimer hopping integral s , the intra-dimer hopping integrals t_1 and t_2 are represented by the horizontal thin black lines, the vertical thick red line, and the vertical thin blue line, respectively. The up (down) spin polarizations are described by the yellow upward (purple downward) arrows. (b) Band structures of the Hamiltonian defined in Eq. (2). We take $t_1 = 1.0$, $t_2 = 0.6$, $s = 0.6$, $\delta = 0.2$, and $\Delta = 1.5$. For comparison, we also show the band structures of the equivalent dimer case with the broken curves, whose parameters are given by $t_1 = t_2 = 1.0$, $s = 0.6$, $\delta = 0.0$, and $\Delta = 1.5$.

ferrimagnets, a simple method to realize them is necessary.

In this Letter, we present a path towards fully compensated ferrimagnets with colossal spin splitting using typical dimer structures in organic compounds. Using a simple one-dimensional model, we demonstrate that a collinear antiferromagnetic order with inequivalent dimers can induce fully compensated ferrimagnets. Furthermore, we find that the recently discovered organic compound (EDO-TTF-I)₂ClO₄ [EDO-TTF-I=4,5-ethylenedioxy-4'-iodotetrathiafulvalene] [23] can realize this mechanism based on *ab initio* calculations. The experiments demonstrate that (EDO-TTF-I)₂ClO₄ under-

goes a structural transition with anionic ordering at 190 K. Below the structural transition, unit-cell doubling occurs with the extended unit cell containing two inequivalent dimers. By deriving and solving the *ab initio* effective Hamiltonian for the low-temperature phase of (EDO-TTF-I)₂ClO₄, we find that the ground state is a collinear antiferromagnet with isotropic spin splitting, i.e., a fully compensated ferrimagnet.

Simple model.—First, to show the key idea for realizing the compensated ferrimagnets, we consider a one-dimensional model whose unit cell contains two *inequivalent* dimers. A schematic of the model is illustrated in Fig. 1 (a). The inequivalence between the two dimers is characterized using difference between the intra-dimer hoppings t_1 and t_2 and chemical potential difference δ . We also consider the collinear dimer antiferromagnetic (DAF) state, where the up-(down-)spin electrons are located on A and A' (B and B'). This DAF state is not invariant to any combination of time reversal with translation/rotation operations because of dimer inequivalence. Thus, isotropic spin splitting is expected in this dimer collinear DAF state.

To determine the mechanism of spin splitting in this model, we consider the following tight-binding Hamiltonian for the DAF state:

$$\mathcal{H} = \sum_{k,\sigma} c_{k\sigma}^\dagger H_\sigma(k) c_{k\sigma}, \quad (1)$$

$$H_\sigma(k) = \begin{pmatrix} \sigma\Delta & t_1 & A(k) & 0 \\ t_1 & \sigma\Delta & 0 & A(k) \\ A(k)^* & 0 & -\sigma\Delta + \delta & t_2 \\ 0 & A(k)^* & t_2 & -\sigma\Delta + \delta \end{pmatrix}, \quad (2)$$

where $c_{k\sigma}^\dagger = (c_{Ak\sigma}^\dagger, c_{A'k\sigma}^\dagger, c_{Bk\sigma}^\dagger, c_{B'k\sigma}^\dagger)$, $A(k) = s(1 + e^{-ik})$ and Δ denotes the gap induced by the DAF order. The spin index σ takes +1 and -1 for the up- and down-spins, respectively. The eigenvalues of this Hamiltonian are given by

$$E_{0,\sigma,\pm}(k) = \delta/2 + t_\pm \pm [(\sigma\Delta + t_- - \delta/2)^2 + 2s^2C(k)]^{1/2}, \quad (3)$$

$$E_{1,\sigma,\pm}(k) = \delta/2 - t_\pm \pm [(\sigma\Delta - t_- - \delta/2)^2 + 2s^2C(k)]^{1/2}, \quad (4)$$

where $t_\pm = (t_1 \pm t_2)/2$ and $C(k) = (1 + \cos k)$. Thus, spin splitting of the bands is induced by $t_- = (t_1 - t_2)/2$ and δ , i.e., inequivalence of the dimers. From these expressions, it is evident that the differences in intra-dimer hoppings have the similar gap-opening effect as the differences in the chemical potentials. Because t_- and δ are independent of the wave number, spin splitting is isotropic.

Figure 1(b) shows the electronic band structures of the Hamiltonian defined in Eq. (2) for a typical parameter set. We also plot the band structures when the two dimers are equivalent ($t_1 = t_2$ and $\delta = 0$). As expected,

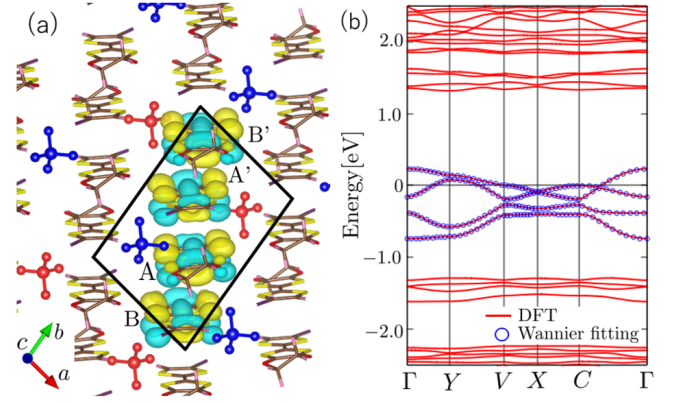


FIG. 2. (a) Crystal structure of (EDO-TTF-I)₂ClO₄ at $T = 100$ K and the real-space distribution of maximally localized Wannier functions (MLWFs) drawn by VESTA [24]. Anions ClO₄ are represented by balls and rods. Colors of anions represent their orientations. Due to the different configurations of anions around the dimers, two dimers (A-A' and B-B') become inequivalent. Black lines show the unit cell including four molecules. (b) Energy band structure obtained by the DFT calculation (red lines) and the MLWFs (blue circles) for the paramagnetic states. The Fermi energy is set to zero.

isotropic spin splitting occurs in the band structures. At commensurate filling (i.e., three-quarter, half, and quarter filling), the DAF state is insulating, and the net magnetization is zero because the number of up- and down-bands below the Fermi energy are the same. Thus, the DAF state at the commensurate filling is the fully compensated ferrimagnets with isotropic spin splitting.

Crystal and electronic structures of (EDO-TTF-I)₂ClO₄.—First, we summarize the crystal structure of (EDO-TTF-I)₂ClO₄. (EDO-TTF-I)₂ClO₄ consists of EDO-TTF-I molecule with +1/2 charge (3/4 filling) and anion ClO₄ layers. Above 190 K, the unit cell contains two EDO-TTF-I molecules and space inversion symmetry is macroscopically protected because of the random orientation of ClO₄. By lowering the temperature, the structural phase transition with anion ordering occurs at approximately $T = 190$ K, which induces unit-cell doubling, as evidenced by the X-ray analysis. As shown in Fig. 2 (a), each unit cell contains four molecules in the low-temperature phase. A and A' (B and B') molecules in a unit cell form a dimer, referred to as dimer I (dimer II). The inversion centers are at the centers of each dimer. The inequivalence of the dimers I and II can also be understood from the partial density of states (PDOS), which are shown in the Supplemental Material [25]. Because dimers I and II are inequivalent after the structural phase transition, (EDO-TTF-I)₂ClO₄ will exhibit compensated ferrimagnetism if appropriate antiferromagnetic order occurs. We note the related organic compound (EDO-TTF-I)₂PF₆ [26] has similar crystal structures; however, all the dimers are equivalent.

This indicates that the ordering of ClO_4 plays an essential role in realizing inequivalent dimers.

Next, we summarize the low-temperature electronic structure of $(\text{EDO-TTF-I})_2\text{ClO}_4$. Although the resistivity exhibits semimetallic behavior immediately after the structural phase transition, a metal-insulator phase transition occurs at approximately $T = 95$ K [23]. It is confirmed that the metal-insulator transition does not accompany a structural change. As explained later, *ab initio* analysis suggests that the DAF ordering is the origin of the insulating phase although the origin of the metal-insulator transition is not experimentally clarified yet.

Ab initio effective Hamiltonian for (EDO-TTF-I)₂ClO₄.— To investigate the electronic structures of the low-temperature phase in $(\text{EDO-TTF-I})_2\text{ClO}_4$, we derive the *ab initio* low-energy effective Hamiltonian, based on band structures obtained by the density functional theory (DFT). We use Quantum ESPRESSO [27] to obtain the DFT bands. In this study, we employ the optimized norm-conserving Vanderbilt pseudopotentials and plane-wave basis sets [28, 29]. The exchange-correlation functional used in this study is the generalized gradient approximation proposed by Perdew, Burke, and Ernzerhof [30]. The cut-off energy of the wave functions and charge densities are set to be 80 Ry and 320 Ry, respectively. During the self-consistent loop process, a $5 \times 5 \times 3$ uniform \mathbf{k} -point grid and Methfessel-Paxton smearing method are used [31]. We use the crystal structure data at 100 K [23]. We perform structural optimization for hydrogen atoms and use the optimized structure in the following analyses. In the DFT calculations, we only consider the paramagnetic solutions. Figure 2 (b) shows the obtained energy band structures of $(\text{EDO-TTF-I})_2\text{ClO}_4$. The four bands around the Fermi level, which are isolated from the other bands, mainly consist of the highest occupied molecular orbitals of the four EDO-TTF-I molecules in the unit cell (A, A', B, and B'). We select these four bands as the low-energy degrees of freedom and use them to construct the maximally localized Wannier functions (MLWFs) using RESPACK [32]. Isosurfaces of the MLWFs are shown in Fig.2 (a). In addition, we confirm that the bands interpolated by the MLWFs accurately reproduce the DFT band structures (Fig.2 (b)).

After constructing MLWFs, we derive low-energy effective Hamiltonian, which is given by

$$\begin{aligned} H_{\text{EDO}} &= H_0 + H_{\text{int}}, \\ H_0 &= \sum_{i,j,\alpha,\beta,\sigma} t_{i\alpha j\beta} c_{i\alpha\sigma}^\dagger c_{j\beta\sigma}, \\ H_{\text{int}} &= \sum_{i,\alpha} U_{i\alpha} n_{i\alpha\uparrow} n_{i\alpha\downarrow} + \frac{1}{2} \sum_{i,j,\alpha,\beta} V_{i\alpha j\beta} N_{i\alpha} N_{j\beta}, \end{aligned} \quad (5)$$

where $c_{i\alpha\sigma}^\dagger$ ($c_{i\alpha\sigma}$) is a creation (annihilation) operator for an electron in the i -th unit cell with orbitals $\alpha = \text{A,}$

A' , B , B' and spin σ . The number operators are defined as $n_{i\alpha\sigma} = c_{i\alpha\sigma}^\dagger c_{i\alpha\sigma}$ and $N_{i\alpha} = n_{i\alpha\uparrow} + n_{i\alpha\downarrow}$. The transfer integrals $t_{i\alpha j\beta}$ are evaluated using the MLWFs. We also evaluate the screened Coulomb interactions $U_{i\alpha}$ and $V_{i\alpha j\beta}$ using the constrained random phase approximation [33, 34] implemented in RESPACK [32]. We set the cutoff energy of the polarization function to 5.0 Ry. Details of the transfer integrals and interaction parameters are summarized in the Supplemental Material [25]. We note that the difference in the intra-dimer hoppings t_1 and t_2 and the existence of the site potential δ indicate the inequivalence of the dimers. In actual calculations, we subtract a constant value Δ_{DDF} from onsite and offsite Coulomb interactions to consider the interlayer screening [35, 36]. Following previous studies [36–39], we employ $\Delta_{\text{DDF}} = 0.2$ eV. We confirm that the results are insensitive to Δ_{DDF} . We also perform an electron-hole transformation to reduce the numerical cost.

many-variable variational Monte Carlo (mVMC) analysis.— The effective Hamiltonian is solved using the mVMC method [40, 41], which can take into account quantum fluctuations and spatial correlations seriously. The trial wave function used in this study is given by

$$|\psi\rangle = \mathcal{P}_G \mathcal{P}_J \mathcal{L}_S |\phi_{\text{pair}}\rangle, \quad (6)$$

$$\mathcal{P}_G = \exp \left[\sum_i g_i n_{i\uparrow} n_{i\downarrow} \right], \quad (7)$$

$$\mathcal{P}_J = \exp \left[\frac{1}{2} \sum_{i \neq j} v_{ij} N_i N_j \right], \quad (8)$$

$$|\phi_{\text{pair}}\rangle = \left[\sum_{i,j}^{N_{\text{site}}} f_{ij} c_{i\uparrow}^\dagger c_{j\downarrow}^\dagger \right]^{N_e/2} |0\rangle, \quad (9)$$

where \mathcal{P}_G , \mathcal{P}_J , and \mathcal{L}_S are the Gutzwiller factor [42], long-range Jastrow factor [43, 44], and total spin projector [45, 46], respectively [41, 47]. N_e and N_{site} indicate the number of electrons and sites, respectively. We impose a 1×4 sublattice structure on variational parameters. We use the Hartree-Fock approximation results as the initial f_{ij} values. The spin-singlet projection ($S = 0$) is used in ground-state calculations for $L_a = L_b \leq 8$, while it is not used for $L_a = L_b \geq 10$ to reduce the numerical costs. We confirm that the spin projection does not largely affect physical quantities, such as the spin structure factors. All variational parameters are simultaneously optimized using the stochastic reconfiguration method [48].

As detailed in the Supplementary Materials, the Hartree-Fock approximation shows that the DAF state (Fig.3 (a)) and antiferromagnetic states with charge ordering (AF+CO) are ground state candidates. Within the Hartree-Fock approximation, the ground state of the effective Hamiltonian is the AF+CO state. However, using the mVMC method, we find that the DAF state be-

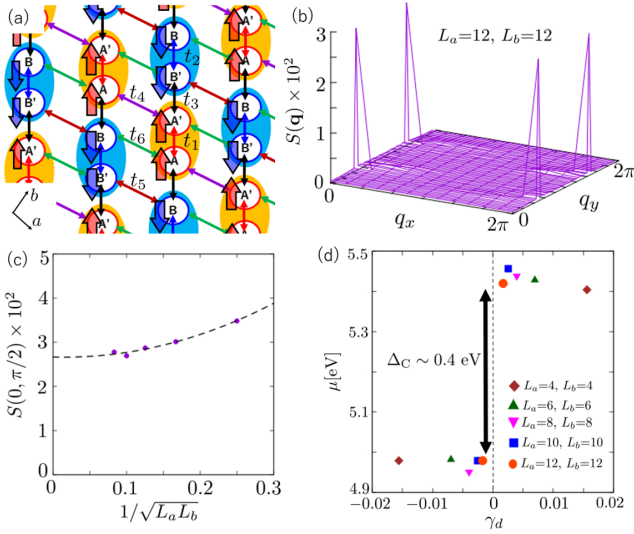


FIG. 3. (a) Schematic of the DAF state and representative hopping integrals (t_1 - t_6) in the conducting layer of (EDO-TTF-I) $_2$ ClO $_4$. (b) Spin structure factor obtained by the mVMC method for $L_a = L_b = 12$. Sharp peaks appear at $\mathbf{q} = (0, \pi/2), (0, 3\pi/2)$, which correspond to the DAF state. (c) Size dependence of the peak value of the spin structure factors. (d) Doping dependence of the chemical potential.

comes the ground state of the effective Hamiltonian. We also find that the AF+CO state converges to the DAF state after optimization, even when using the variational parameters of AF+CO state as the initial state. This result indicates that correlation effects beyond the mean-field approximation are important in stabilizing the DAF state.

To examine the existence of long-range antiferromagnetic order, we calculate the spin-correlation functions of the ground state, defined as

$$S(\mathbf{q}) = \frac{1}{(N_{\text{site}})^2} \sum_{i,j} \langle \mathbf{S}_i \cdot \mathbf{S}_j \rangle e^{i\mathbf{q} \cdot (\mathbf{r}_i - \mathbf{r}_j)}, \quad (10)$$

where the original lattice structure is mapped to the equivalent $L_a \times 4L_b$ square lattice for simplicity. Figure 3 (b) shows $S(\mathbf{q})$ in the momentum space, with sharp Bragg peaks at $(q_x, q_y) = (0, \pi/2)$ and $(0, 3\pi/2)$. As shown in Fig. 3 (c), we confirm that the peak values of $S(\mathbf{q})$ remain finite in the thermodynamic limit. We also confirm that charge densities are uniform and there is no signature of a charge-ordered state. These results show that the ground state of the effective Hamiltonian is the DAF state. In addition, we calculate the charge gap Δ_c , given by $\Delta_c = \mu(N_e + 1) - \mu(N_e - 1)$, where the chemical potential is defined as $\mu(N_e + 1) = [E(N_e + 2) - E(N_e)]/2$. Figure 3 (d) shows the doping rate $\gamma_d = N_e/N_{\text{site}} - 1.5$ dependence of the chemical potential. From this plot, we estimate the charge gap $[\Delta_c = \mu(N_e + 1) - \mu(N_e - 1)]$ as $\Delta_c \sim 0.4$ eV. This result indicates that the ground state

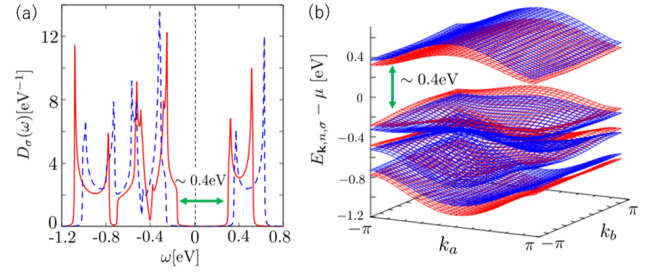


FIG. 4. (a) Density of state (DOS) of the low-energy effective Hamiltonian (EDO-TTF-I) $_2$ ClO $_4$ for the DAF state obtained by the Hartree-Fock approximation. DOS for up (down) spin is described by the red (blue) lines. (b) Band dispersions of the DAF state obtained by the Hartree-Fock approximation. The red (blue) surfaces describe up-spin (down-spin) band dispersions.

of (EDO-TTF-I) $_2$ ClO $_4$ is the DAF insulator.

Spin splitting.—Based on the results obtained using the mVMC method, we analyze spin splitting in the DAF state using the Hartree-Fock approximation (for more details, see Ref. [25]). We assume the DAF order and scale the interaction parameters to reproduce the charge gap $\Delta_c \sim 0.4$ eV obtained from the mVMC calculations. The scaling ratio λ , which monotonically scales the onsite and offsite Coulomb interactions, is estimated to be $\lambda = 0.7$. The details of the Hartree-Fock calculations are provided in the Supplemental Material.

Using the Hartree-Fock approximation, we calculate the DOS defined as $D_\sigma(\omega) = (\pi L_a L_b)^{-1} \sum_{\mathbf{k}, n} \text{Im}(\omega - i\eta - E_{\mathbf{k}, n, \sigma} + \mu)^{-1}$, where μ and η are the chemical potential and the smearing factor, respectively. $E_{\mathbf{k}, n, \sigma}$ denotes the n -th eigenvalue of the mean-field Hamiltonian at momentum \mathbf{k} . We set $\eta = 0.002$ eV. As shown in Fig. 4 (a), spin splitting occurs in the DAF order ($D_\uparrow(\omega) \neq D_\downarrow(\omega)$). The electronic band dispersions in Fig. 4(b) also show isotropic spin splitting over the entire Brillouin zone. This demonstrates that (EDO-TTF-I) $_2$ ClO $_4$ can be fully compensated ferrimagnets if a DAF order occurs.

Here, we analyze the origin of spin splitting in (EDO-TTF-I) $_2$ ClO $_4$. As in the case of the simple model, $t_- = (t_1 - t_2)/2$ and δ can induce spin splitting. From the *ab initio* calculations, we find that $t_- = 0.036$ eV is comparable to $\delta = 0.047$ eV. Thus, spin splitting in (EDO-TTF-I) $_2$ ClO $_4$ is induced by both t_- and δ . One might think that finite δ would make the total magnetization finite; however, a charge gap guarantees that the total magnetization is robust against perturbations. In this case, the total magnetization is zero at $\delta = 0$ and remains zero even if δ is added, provided that δ is significantly smaller than the charge gap.

Summary and discussion.—In this Letter, we present a simple method to realize fully compensated ferrimagnetism using the dimer degrees of freedom, which are

typical of organic compounds. Using a simple model, we demonstrate that the inequivalence of the two dimers and DAF order can induce fully compensated ferrimagnets at commensurate filling. Furthermore, *ab initio* calculations suggest that the ground state of $(\text{EDO-TTF-I})_2\text{ClO}_4$ is a DAF insulator with inequivalent dimers. As a result, the DAF order induces isotropic spin splitting in the electronic band structure. Our study shows that the key to realizing compensated ferrimagnetism lies in inequivalent dimer structures induced by anion ordering. This finding offers an unanticipated direction in materials design, where exotic magnetism can be achieved by selecting and modifying anions to exhibit anion ordering. The discovery of compensated ferrimagnetism in inequivalent dimer structures, as well as the potential for materials design using anion ordering, demonstrates that organic compounds offer a versatile platform for realizing exotic magnetism. An intriguing future issue would be to examine the doping effects in the DAF insulating state. Because the lowest unoccupied band is fully polarized and its DOS is large (Fig.4 (a)), unconventional superconductivity, such as triplet superconductivity, is expected [49]. Further experimental and theoretical investigations in this direction are desirable.

The authors thank Y. Nakano, M. Ishikawa, H. Yamochi, and A. Otsuka for the fruitful discussions. This work was financially supported by Grants-in-Aid for Scientific Research (KAKENHI) (Grant Nos. 23H03818, 23KJ1065, 15K05166, 22K18683 21H01793), Grant-in-Aid for Scientific Research for Transformative Research Areas (A) “Condensed Conjugation” (No. JP20H05869) from Japan Society for the Promotion of Science (JSPS), and JST SPRING (Grant No. JPMJSP2125). The computations were performed using the facilities at the Supercomputer Center, Institute for Solid State Physics, University of Tokyo.

Supplemental Material for “Compensated Ferrimagnets with Colossal Spin Splitting in Organic Compounds”

PARAMETERS IN *AB INITIO* LOW-ENERGY EFFECTIVE HAMILTONIANS

We calculate the electronic band structures by the density functional theory (DFT) using Quantum ESPRESSO [27] and evaluate the transfer integrals by the maximally localized Wannier functions (MLWFs). Then, we evaluate Coulomb interaction by the constraint random phase approximation (cRPA) using RESPACK [32]. The values of the transfer integrals larger than 0.020 eV and the Coulomb interactions are shown in Table I. We show schematic illustrations of the transfer integrals and the Coulomb interactions in Fig. 5. All input and output files are uploaded to the ISSP data repository [50].

Transfer integrals [eV]		Coulomb interactions [eV]	
δ	0.047	$U_A=U_{A'}$	2.094
		$U_B=U_{B'}$	2.076
t_1	0.252	V_1	0.903
t_2	0.179	V_2	0.884
t_3	0.128	V_3	0.880
t_4	0.112	V_4	0.700
t_5	0.084	V_5	0.681
t_6	0.058	V_6	0.614
t_7	-	V_7	0.659
t_8	-	V_8	0.628

TABLE I. Transfer integrals and screened Coulomb interactions of the *ab initio* low-energy effective Hamiltonians for (EDO-TTF-I)₂ClO₄.

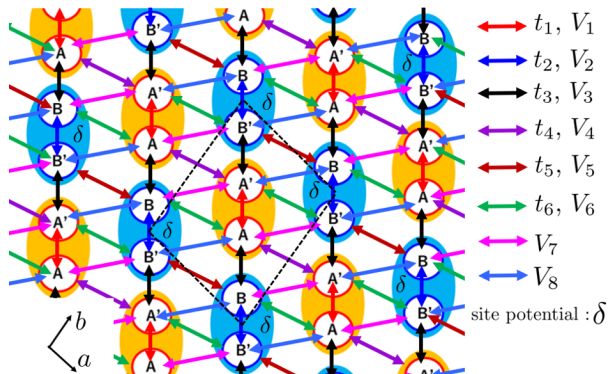


FIG. 5. Schematic of the transfer integrals and the off-site Coulomb interactions in the conduction layer.

PARTIAL DENSITIES OF STATES

To see the inequivalence of the dimers, we calculate the partial densities of states (PDOS) using the one-body part of the low-energy effective Hamiltonians for (EDO-TTF-I)₂ClO₄ in the momentum space, which is given by

$$\begin{aligned} H_\sigma^0(\mathbf{k}) &= \sum_{\mathbf{k}} \sum_{\Delta\mathbf{r},\alpha,\beta} t_{\Delta\mathbf{r},\alpha\beta} e^{i\mathbf{k}\cdot\Delta\mathbf{r}} c_{\mathbf{k},\alpha,\sigma}^\dagger c_{\mathbf{k},\beta,\sigma} \\ &= \sum_{\mathbf{k}} \sum_{\Delta\mathbf{r},\alpha,\beta} H_{\alpha\beta,\sigma}^0(\mathbf{k}) c_{\mathbf{k},\alpha,\sigma}^\dagger c_{\mathbf{k},\beta,\sigma}. \end{aligned} \quad (11)$$

Here, $t_{\Delta\mathbf{r},\alpha\beta}$ is the transfer integrals obtained by RESPACK and $\Delta\mathbf{r}$ represents the translational vector. The Hamiltonian $H_\sigma^0(\mathbf{k})$ satisfies the following eigenvalue equation:

$$H_\sigma^0(\mathbf{k}) |\mathbf{k}, n, \sigma\rangle = E_{n,\sigma}(\mathbf{k}) |\mathbf{k}, n, \sigma\rangle, \quad (12)$$

$$|\mathbf{k}, n, \sigma\rangle = \begin{pmatrix} d_{A,n,\sigma}(\mathbf{k}) \\ d_{A',n,\sigma}(\mathbf{k}) \\ d_{B,n,\sigma}(\mathbf{k}) \\ d_{B',n,\sigma}(\mathbf{k}) \end{pmatrix}, \quad (13)$$

where $E_{n,\sigma}(\mathbf{k})$ and $|\mathbf{k}, n, \sigma\rangle$ are the eigenvalue and eigenvectors of H^0 . The band and spin indices are represented by n and σ , respectively. Using $E_{n,\sigma}(\mathbf{k})$ and $d_{\alpha,n,\sigma}(\mathbf{k})$, the PDOS $D_\alpha(\omega)$ can be calculated as

$$D_\alpha(\omega) = \frac{1}{\pi L_a L_b} \sum_{\mathbf{k}, n, \sigma} \text{Im} \frac{|d_{\alpha,n,\sigma}(\mathbf{k})|^2}{\omega - i\eta - E_{\mathbf{k},n,\sigma} + \mu}, \quad (14)$$

where η takes the positive infinitesimal value and μ is the chemical potential determined to set the electron number to 6. We set $\eta = 0.002$ eV in the numerical calculation. Figure 6 shows the PDOS $D_\alpha(\omega)$. We consider the paramagnetic state in this calculation. The inequivalence in $D_A(\omega)$ and $D_B(\omega)$ indicates the inequivalence of the dimer I and II. We note that the relations $D_A(\omega) = D_{A'}(\omega)$ and $D_B(\omega) = D_{B'}(\omega)$ are satisfied due to space-inversion symmetry.

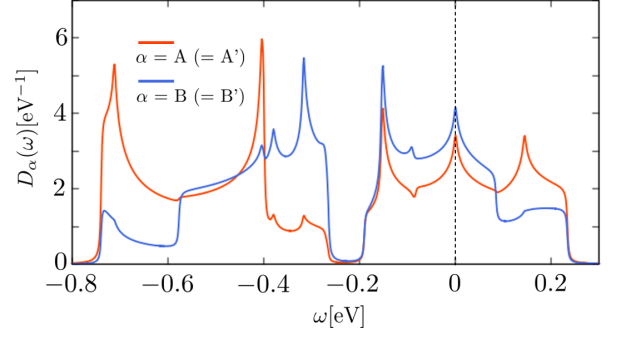


FIG. 6. PDOS obtained by the tight-binding model. Inequivalence of the dimers appears in the PDOS ($D_A(\omega) \neq D_B(\omega)$).

DETAILS OF THE HARTREE-FOCK APPROXIMATION

To examine the ground state candidates of (EDO-TTF-I)₂ClO₄, we perform the Hartree-Fock (HF) approximation to the *ab initio* low-energy effective Hamiltonians defined in Eq. (5) in the main text. We use the unrestricted HF code implemented in mVMC [41]. Using the results of HF calculations, we generate the initial variational parameters for the mVMC method. In this study, we examine the ordered states with $\mathbf{q} = 0$, i.e., we consider the symmetry-broken states within the unit cell. As illustrated in Fig. 7, we consider five initial states: (i) the paramagnetic (PM) state, (ii) the ferromagnetic (FM) state, (iii) the dimer antiferromagnetic (DAF) state, (iv) the AF state, (v) the AF state with charge ordering (AF+CO). To examine the correlation effects, we introduce the parameter λ , which monotonically scales the Coulomb interactions as $\tilde{U}_{i\alpha} \equiv \lambda(U_{i\alpha} - \Delta_{\text{DDF}})$ and $\tilde{V}_{i\alpha j\beta} \equiv \lambda(V_{i\alpha j\beta} - \Delta_{\text{DDF}})$. Here, Δ_{DDF} denotes the constant shift that takes into account the screening effects between conduction layers [35, 36].

Figures 8 (a) and (b) show the charge density $\langle n_i^C \rangle = \langle n_{i\uparrow} + n_{i\downarrow} \rangle$ and the spin density $\langle n_i^S \rangle = \langle n_{i\uparrow} - n_{i\downarrow} \rangle$ at the i th (=A, A', B, B') site in the ground states obtained by the HF approximation for $\Delta_{\text{DDF}} = 0.2$ eV, respectively. We find that the PM state [$\langle n_{A(B)}^C \rangle = \langle n_{A'(B')}^C \rangle$ and $\langle n_i^S \rangle = 0$] is the ground state below $\lambda \sim 0.3$. In $0.3 \lesssim \lambda \lesssim 0.5$, DAF state [$\langle n_{A(B)}^C \rangle = \langle n_{A'(B')}^C \rangle$ and $\langle n_A^S \rangle = \langle n_{A'}^S \rangle = -\langle n_B^S \rangle = -\langle n_{B'}^S \rangle$] becomes the ground state. For $\lambda \gtrsim 0.5$, the AF state with the CO [$\langle n_{A(B')}^C \rangle > \langle n_{A'(B)}^C \rangle$ and $\langle n_{A'(B')}^S \rangle > \langle n_{A(B)}^S \rangle$] becomes the ground state. Figure 8 (c) shows the λ - Δ_{DDF} phase diagram. Since amplitudes of the on-site and off-site Coulomb interactions become small with increasing Δ_{DDF} , the phase boundary between the DAF state and the AF+CO state slightly shifts to large λ region by increasing Δ_{DDF} .

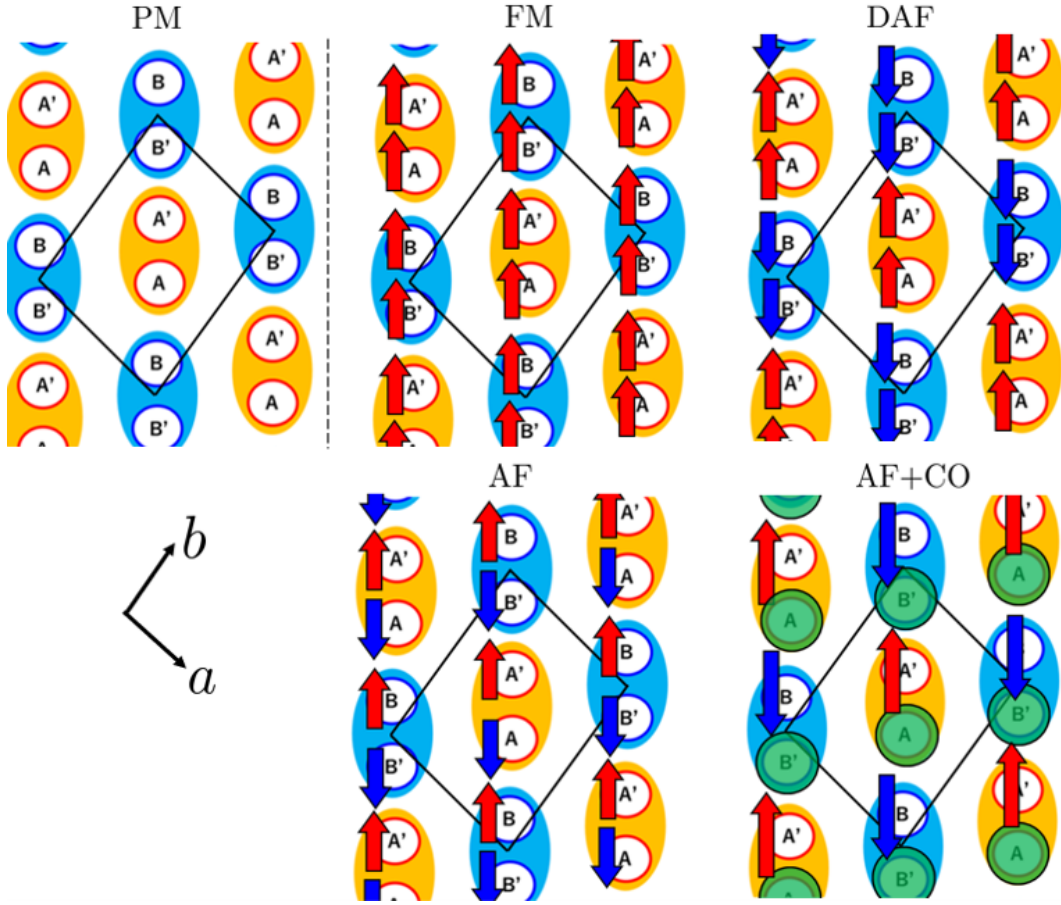


FIG. 7. Schematic illustrations of initial states used in the HF approximation. The up and down arrows indicate the spin-up and spin-down states, respectively. The orange and blue ellipses represent the dimer states constructed by A-A' molecules and B-B' molecules, respectively. The green circles represent the charge-rich sites.

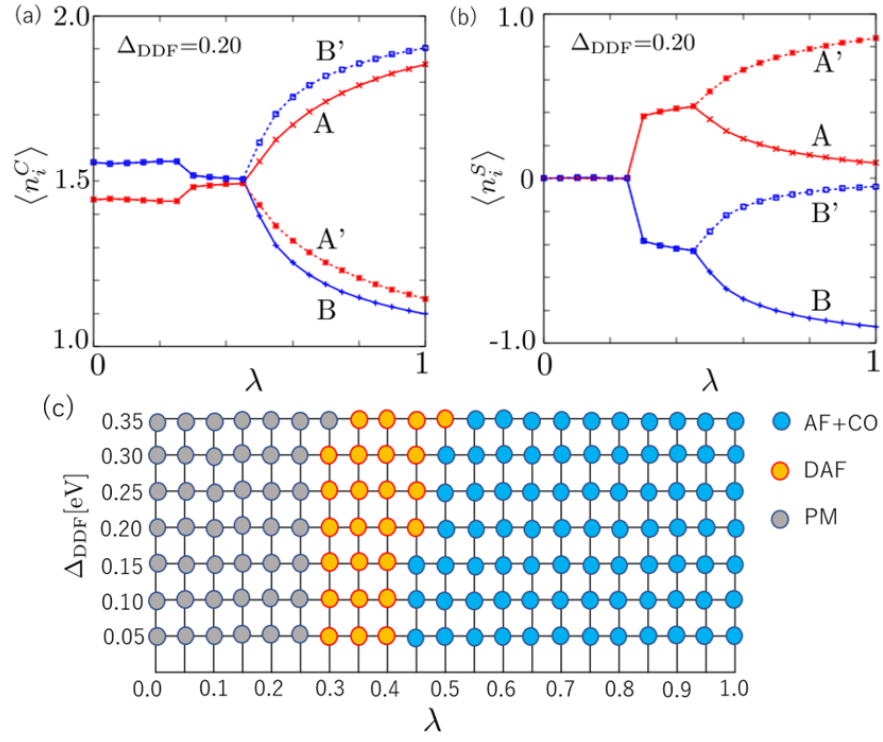


FIG. 8. λ dependence of (a) the charge density and (b) the spin density. (c) λ - Δ_{DDF} phase diagram obtained by the HF approximation.

MVMC ANALYSIS OF THE GROUND-STATE PHASE DIAGRAM

Based on the results obtained by the HF calculations, we investigate the ground states using the mVMC method, which can treat correlation effects more accurately. Following previous studies [36–39], we take $\Delta_{\text{DDF}} = 0.20$ eV. Figure 9(a) shows the phase diagram as a function of λ . By increasing λ , the phase transition between the DAF state and the PM state occurs around $\lambda = 0.5$. Above $\lambda \sim 2.2$, the AF+CO state becomes the ground state due to the off-site Coulomb interactions. Figure 9(b) shows the energy difference between the PM state (the AF+CO state) and the DAF state, i.e., $\Delta E_1 = E_{\text{PM}} - E_{\text{DAF}}$ ($\Delta E_2 = E_{\text{AF+CO}} - E_{\text{DAF}}$) as a function of λ for $L_a = L_b = 6$ lattice. The AF+CO state is a quasi-stable state for $\lambda \gtrsim 1.4$ and becomes the ground state for $\lambda \gtrsim 2.2$. We note that the AF+CO state is not stabilized even when we select the AF+CO state as an initial state for $\lambda \lesssim 1.2$. Figure 10 shows the spin and charge density structure factors of the PM, the DAF, and the AF+CO states. The charge structure factor is defined by

$$N(\mathbf{q}) = \frac{1}{(N_{\text{site}})^2} \sum_{i,j} \langle (N_i - \bar{N}) \cdot (N_j - \bar{N}) \rangle e^{i\mathbf{q} \cdot (\mathbf{r}_i - \mathbf{r}_j)}, \quad (15)$$

$$\bar{N} = \frac{1}{N_{\text{site}}} \sum_i \langle N_i \rangle. \quad (16)$$

The ordering wave vectors $\mathbf{q} = (0, \pi/2), (0, 3\pi/2)$ in $S(\mathbf{q})$ (Fig. 10 (b)) correspond to the DAF state. Meanwhile, the ordering wave vectors $\mathbf{q} = (0, \pi/2), (0, 3\pi/2)$ in $S(\mathbf{q})$ and $\mathbf{q} = (0, \pi)$ in $N(\mathbf{q})$ (Fig. 10(c) and (f)) correspond to the AF+CO state.

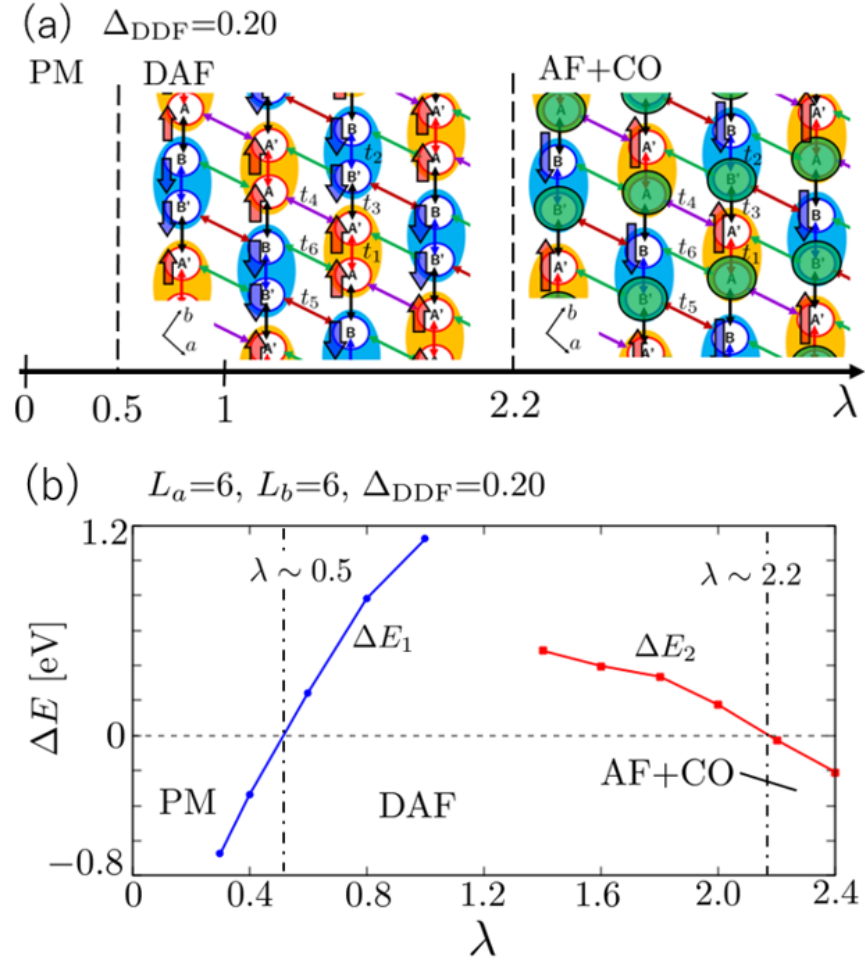


FIG. 9. (a) The ground state phase diagram as a function of λ obtained by the mVMC calculation. (b) λ -dependencies of the energy difference between the PM state and the DAF state (ΔE_1) and the one between the AF+CO state and the DAF state (ΔE_2).

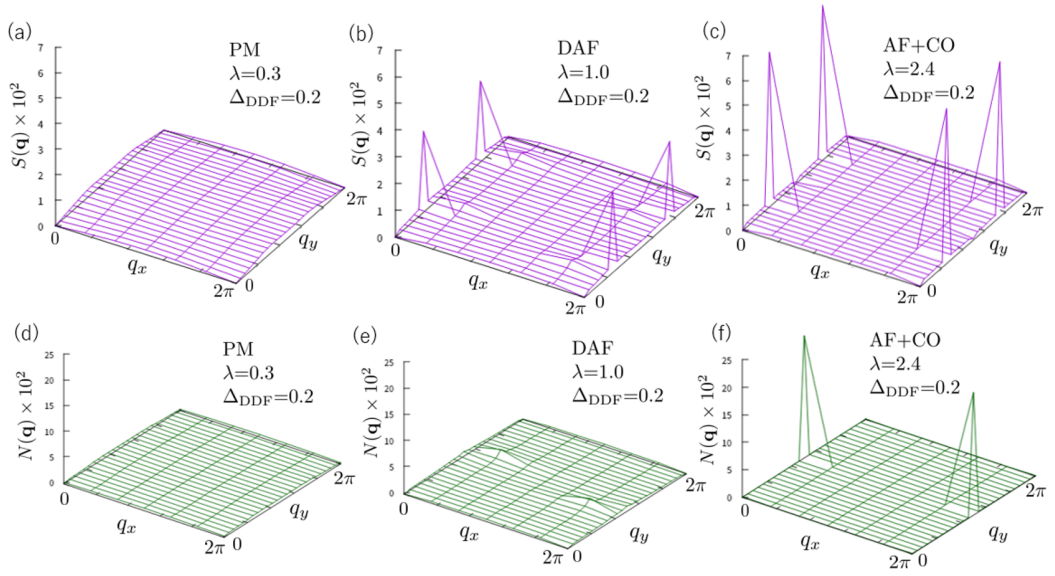


FIG. 10. Spin structure factors $S(\mathbf{q})$ [charge structure factors $N(\mathbf{q})$] of the PM state ($\lambda = 0.3$), the DAF state ($\lambda = 1$), and the AF+CO state ($\lambda = 2.4$) in (a), (b), and (c) [(d), (e), and (f)], respectively.

MEAN-FIELD HAMILTONIAN IN THE MOMENTUM SPACE

To see the spin splitting of the DAF states, we calculate band dispersions and DOS using the one-body Green functions obtained by the HF approximation. Here, we set $\lambda = 0.7$, which reproduces the charge gap estimated by the mVMC method. By performing the Fourier transformation for the mean-field Hamiltonian in the real space, we obtain the mean-field Hamiltonian in the momentum space, which is given by

$$\begin{aligned}
 H = & \sum_{\mathbf{k}} \sum_{\Delta\mathbf{r},\alpha,\beta,\sigma} t_{\Delta\mathbf{r},\alpha\beta} e^{i\mathbf{k}\cdot\Delta\mathbf{r}} c_{\mathbf{k},\alpha,\sigma}^\dagger c_{\mathbf{k},\beta,\sigma} \\
 & + \sum_{\mathbf{k}} \sum_{\alpha,\sigma} U_\alpha \langle n_{\alpha,\bar{\sigma}} \rangle c_{\mathbf{k},\alpha,\sigma}^\dagger c_{\mathbf{k},\alpha,\sigma} \\
 & + \sum_{\mathbf{k}} \sum_{\Delta\mathbf{r},\alpha,\beta,\sigma} V_{\Delta\mathbf{r},\alpha\beta} \langle N_\beta \rangle c_{\mathbf{k},\alpha,\sigma}^\dagger c_{\mathbf{k},\alpha,\sigma} \\
 & - \sum_{\mathbf{k}} \sum_{\Delta\mathbf{r},\alpha,\beta,\sigma} V_{\Delta\mathbf{r},\alpha\beta} \left\langle c_{\mathbf{r}_0+\Delta\mathbf{r},\beta,\sigma}^\dagger c_{\mathbf{r}_0,\alpha,\sigma} \right\rangle e^{i\mathbf{k}\cdot\Delta\mathbf{r}} c_{\mathbf{k},\alpha,\sigma}^\dagger c_{\mathbf{k},\beta,\sigma}.
 \end{aligned} \tag{17}$$

Here, $\Delta\mathbf{r}$ denotes the translational vector and $\bar{\sigma} = -\sigma$. Off-diagonal one-body Green functions in the real space are represented by $\langle c_{\mathbf{r}_0+\Delta\mathbf{r},\beta,\sigma}^\dagger c_{\mathbf{r}_0,\alpha,\sigma} \rangle$. We take $\mathbf{r}_0 = \mathbf{0}$ as the representative coordinate of \mathbf{r}_0 because \mathbf{r}_0 is an arbitrary coordinate due to translational symmetry. Using the mean-field Hamiltonians in the momentum space, we calculate the band dispersions and the DOS. All values of the one-body Green functions are uploaded to the ISSP data repository [50].

* tmisawa@issp.u-tokyo.ac.jp

- [1] L. Šmejkal, A. H. MacDonald, J. Sinova, S. Nakatsuji, and T. Jungwirth, Anomalous Hall antiferromagnets, *Nat. Rev. Mater.* **7**, 482 (2022).
- [2] L. Šmejkal, J. Sinova, and T. Jungwirth, Beyond conventional ferromagnetism and antiferromagnetism: A phase with nonrelativistic spin and crystal rotation symmetry, *Phys. Rev. X* **12**, 031042 (2022).
- [3] L. Šmejkal, J. Sinova, and T. Jungwirth, Emerging research landscape of altermagnetism, *Phys. Rev. X* **12**, 040501 (2022).
- [4] I. Mazin (The PRX Editors), Editorial: Altermagnetism—A New Punch Line of Fundamental Magnetism, *Phys. Rev. X* **12**, 040002 (2022).
- [5] Y. Noda, K. Ohno, and S. Nakamura, Momentum-dependent band spin splitting in semiconducting MnO₂: a density functional calculation, *Phys. Chem. Chem. Phys.* **18**, 13294 (2016).
- [6] M. Naka, S. Hayami, H. Kusunose, Y. Yanagi, Y. Motome, and H. Seo, Spin current generation in organic antiferromagnets, *Nat. Commun.* **10**, 1 (2019).
- [7] S. Hayami, Y. Yanagi, and H. Kusunose, Momentum-dependent spin splitting by collinear antiferromagnetic ordering, *J. Phys. Soc. Jpn.* **88**, 123702 (2019).
- [8] K.-H. Ahn, A. Hariki, K.-W. Lee, and J. Kuneš, Antiferromagnetism in RuO₂ as *d*-wave pomeranchuk instability, *Phys. Rev. B* **99**, 184432 (2019).
- [9] L.-D. Yuan, Z. Wang, J.-W. Luo, E. I. Rashba, and A. Zunger, Giant momentum-dependent spin splitting in centrosymmetric low-*Z* antiferromagnets, *Phys. Rev. B* **102**, 014422 (2020).
- [10] L. Šmejkal, R. González-Hernández, T. Jungwirth, and J. Sinova, Crystal time-reversal symmetry breaking and spontaneous Hall effect in collinear antiferromagnets, *Sci. adv.* **6**, eaaz8809 (2020).
- [11] M. Naka, S. Hayami, H. Kusunose, Y. Yanagi, Y. Motome, and H. Seo, Anomalous Hall effect in κ -type organic antiferromagnets, *Phys. Rev. B* **102**, 075112 (2020).
- [12] M. Naka, Y. Motome, and H. Seo, Perovskite as a spin current generator, *Phys. Rev. B* **103**, 125114 (2021).
- [13] I. I. Mazin, K. Koepernik, M. D. Johannes, R. González-Hernández, and L. Šmejkal, Prediction of unconventional magnetism in doped FeSb₂, *Proc. Natl. Acad. Sci.* **118**, e2108924118 (2021).
- [14] Z. Feng, X. Zhou, L. Šmejkal, L. Wu, Z. Zhu, H. Guo, R. González-Hernández, X. Wang, H. Yan, P. Qin, *et al.*, An anomalous Hall effect in altermagnetic ruthenium dioxide, *Nat. Electron.* **5**, 735 (2022).
- [15] H. van Leuken and R. A. de Groot, Half-Metallic Antiferromagnets, *Phys. Rev. Lett.* **74**, 1171 (1995).
- [16] W. E. Pickett, Spin-density-functional-based search for half-metallic antiferromagnets, *Phys. Rev. B* **57**, 10613 (1998).
- [17] H. Akai and M. Ogura, Half-Metallic Diluted Antiferromagnetic Semiconductors, *Phys. Rev. Lett.* **97**, 026401 (2006).
- [18] S. A. Egorov and R. A. Evarestov, Colossal spin splitting in the monolayer of the collinear antiferromagnet MnF₂, *J. Phys. Chem. Lett.* **12**, 2363 (2021).
- [19] R. Stinshoff, G. H. Fecher, S. Chadov, A. K. Nayak, B. Balke, S. Ouardi, T. Nakamura, and C. Felser, Half-metallic compensated ferrimagnetism with a tunable compensation point over a wide temperature range in the Mn-Fe-V-Al Heusler system, *AIP Adv.* **7**, 105009 (2017).
- [20] R. Stinshoff, A. K. Nayak, G. H. Fecher, B. Balke, S. Ouardi, Y. Skourski, T. Nakamura, and C. Felser, Completely compensated ferrimagnetism and sublattice spin crossing in the half-metallic Heusler compound Mn_{1.5}FeV_{0.5}Al, *Phys. Rev. B* **95**, 060410(R) (2017).
- [21] P. Midhunlal, J. A. Chelvane, D. Prabhu, R. Gopalan, and N. H. Kumar, Mn₂V_{0.5}Co_{0.5}Z (Z= Ga, Al) Heusler alloys: High T_C compensated P-type ferrimagnetism in arc melted bulk and N-type ferrimagnetism in melt-spun ribbons, *J. Magn. Magn. Mater.* **489**, 165298 (2019).
- [22] S. Semboshi, R. Y. Umetsu, Y. Kawahito, and H. Akai, A new type of half-metallic fully compensated ferrimagnet, *Sci. Rep.* **12**, 10687 (2022).
- [23] Y. Nakano, Y. Takahashi, K. Ishida, M. Ishikawa, and H. Yamochi, Private Communication.
- [24] K. Momma and F. Izumi, VESTA 3 for three-dimensional visualization of crystal, volumetric and morphology data, *J. Appl. Crystallogr.* **44**, 1272 (2011).
- [25] See Supplemental Material at [URL_will_be_inserted_by_publisher](#) for details of parameters in the *ab initio* low-energy effective Hamiltonian, the partial density of states, the Hartree-Fock approximation, mVMC analysis of the ground-state phase diagrams, and mean-field

- Hamiltonian in the momentum space, which includes Refs. [27, 32, 35–39, 41, 50].
- [26] Y. Nakano, Y. Takahashi, K. Ishida, M. Ishikawa, H. Yamochi, and M. Uruichi, Crystal structure and physical properties of radical cation salt based on 4,5-ethylenedioxy-4'-iodotetrathiafulvalene (EDO-TTF-I) with iodine bonding ability, *Mater. Chem. Front.* **2**, 752 (2018).
- [27] P. Giannozzi, O. Andreussi, T. Brumme, O. Bunau, M. B. Nardelli, M. Calandra, R. Car, C. Cavazzoni, D. Ceresoli, M. Cococcioni, *et al.*, Advanced capabilities for materials modelling with Quantum ESPRESSO, *J. of Phys.: Cond. Matt.* **29**, 465901 (2017).
- [28] D. R. Hamann, Optimized norm-conserving Vanderbilt pseudopotentials, *Phys. Rev. B* **88**, 085117 (2013).
- [29] M. Schlipf and F. Gygi, Optimization algorithm for the generation of ONCV pseudopotentials, *Comput. Phys. Commun.* **196**, 36 (2015).
- [30] J. P. Perdew, K. Burke, and M. Ernzerhof, aGeneralized Gradient Approximation Made Simple, *Phys. Rev. Lett.* **77**, 3865 (1996).
- [31] M. Methfessel and A. T. Paxton, High-precision sampling for Brillouin-zone integration in metals, *Phys. Rev. B* **40**, 3616 (1989).
- [32] K. Nakamura, Y. Yoshimoto, Y. Nomura, T. Tadano, M. Kawamura, T. Kosugi, K. Yoshimi, T. Misawa, and Y. Motoyama, RESPACK: An ab initio tool for derivation of effective low-energy model of material, *Comp. Phys. Comm.* **261**, 107781 (2021).
- [33] F. Aryasetiawan, M. Imada, A. Georges, G. Kotliar, S. Biermann, and A. I. Lichtenstein, Frequency-dependent local interactions and low-energy effective models from electronic structure calculations, *Phys. Rev. B* **70**, 195104 (2004).
- [34] M. Imada and T. Miyake, Electronic structure calculation by first principles for strongly correlated electron systems, *J. Phys. Soc. Jpn.* **79**, 112001 (2010).
- [35] K. Nakamura, Y. Yoshimoto, Y. Nohara, and M. Imada, Ab initio low-dimensional physics opened up by dimensional downfolding: application to LaFeAsO, *J. Phys. Soc. Jpn.* **79**, 123708 (2010).
- [36] K. Nakamura, Y. Yoshimoto, and M. Imada, Ab initio two-dimensional multiband low-energy models of $\text{EtMe}_3\text{Sb}[\text{Pd}(\text{dmit})_2]_2$ and $\kappa\text{-(BEDT-TTF)}_2\text{Cu}(\text{NCS})_2$ with comparisons to single-band models, *Phys. Rev. B* **86**, 205117 (2012).
- [37] K. Ido, K. Yoshimi, T. Misawa, and M. Imada, Unconventional dual 1D–2D quantum spin liquid revealed by ab initio studies on organic solids family, *npj Quantum Mater.* **7**, 48 (2022).
- [38] D. Ohki, K. Yoshimi, A. Kobayashi, and T. Misawa, Gap opening mechanism for correlated Dirac electrons in organic compounds $\alpha\text{-(BEDT-TTF)}_2\text{I}_3$ and $\alpha\text{-(BEDT-TSeF)}_2\text{I}_3$, *Phys. Rev. B* **107**, L041108 (2023).
- [39] K. Yoshimi, T. Misawa, T. Tsumuraya, and H. Seo, Comprehensive *Ab Initio* Investigation of the Phase Diagram of Quasi-One-Dimensional Molecular Solids, *Phys. Rev. Lett.* **131**, 036401 (2023).
- [40] D. Tahara and M. Imada, Variational Monte Carlo Method Combined with Quantum-Number Projection and Multi-Variable Optimization, *J. Phys. Soc. Jpn.* **77**, 114701 (2008).
- [41] T. Misawa, S. Morita, K. Yoshimi, M. Kawamura, Y. Motoyama, K. Ido, T. Ohgoe, M. Imada, and T. Kato, mVMC—Open-source software for many-variable variational Monte Carlo method, *Comput. Phys. Commun.* **235**, 447 (2019).
- [42] M. C. Gutzwiller, Effect of Correlation on the Ferromagnetism of Transition Metals, *Phys. Rev. Lett.* **10**, 159 (1963).
- [43] R. Jastrow, Many-Body Problem with Strong Forces, *Phys. Rev.* **98**, 1479 (1955).
- [44] M. Capello, F. Becca, M. Fabrizio, S. Sorella, and E. Tosatti, Variational description of mott insulators, *Phys. Rev. Lett.* **94**, 026406 (2005).
- [45] P. Ring and P. Schuck, *The nuclear many-body problem* (Springer Science & Business Media, 2004).
- [46] T. Mizusaki and M. Imada, Quantum-number projection in the path-integral renormalization group method, *Phys. Rev. B* **69**, 125110 (2004).
- [47] F. Becca and S. Sorella, *Quantum Monte Carlo approaches for correlated systems* (Cambridge University Press, 2017).
- [48] S. Sorella, Generalized Lanczos algorithm for variational quantum Monte Carlo, *Phys. Rev. B* **64**, 024512 (2001).
- [49] I. I. Mazin, Notes on altermagnetism and superconductivity, [arXiv:2203.05000](https://arxiv.org/abs/2203.05000) .
- [50] <https://isspns-gitlab.issp.u-tokyo.ac.jp/k-yoshimi/edottf>.